Received: 16 April 2020 | Accepted: 26 July 2020
DOI: 10.1002/hyp.13879

RESEARCH ARTICLE

WILEY

# Analytical solutions to runoff on hillslopes with curvature: numerical and laboratory verification

Dana A. Lapides[1] | Cy David[1] | Anneliese Sytsma[2] | David Dralle[3] | Sally Thompson[4,5]

[1]Department of Earth and Planetary Science, University of California, Berkeley, California
[2]Department of Environmental Design, University of California, Berkeley, California
[3]USDA Forest Service, sPacific Southwest Research Station, Davis, California
[4]Department of Civil and Environmental Engineering, University of California, Berkeley, California
[5]Department of Environmental Engineering, University of Western Australia, Perth, Western Australia

**Correspondence**
Dana A. Lapides, Department of Earth and Planetary Science, University of California, Berkeley, CA.
Email: danalapides@berkeley.edu

**Funding information**
Engineering Research Center for Reinventing the Nation's Urban Water Infrastructure (ReNUWIt); Gledden Foundation at the University of Western Australia's Institute for Advanced Studies; Hellman Foundation; National Science Foundation, Grant/Award Numbers: EAR-1013339, EAR-BSF1632494; Undergraduate Research Apprenticeship Program (URAP) at University of California; University of California Berkeley

## Abstract
Predicting the behavior of overland flow with analytical solutions to the kinematic wave equation is appealing due to its relative ease of implementation. Such simple solutions, however, have largely been constrained to applications on simple planar hillslopes. This study presents analytical solutions to the kinematic wave equation for hillslopes with modest topographic curvature that causes divergence or convergence of runoff flowpaths. The solution averages flow depths along changing hillslope contours whose lengths vary according hillslope width function, and results in a one-dimensional approximation to the two-dimensional flow field. The solutions are tested against both two-dimensional numerical solutions to the kinematic wave equation (in ParFlow) and against experiments that use rainfall simulation on machined hillslopes with defined curvature properties. Excellent agreement between numerical, experimental and analytical solutions is found for hillslopes with mild to moderate curvature. The solutions show that curvature drives large changes in maximum flow rate $q_{peak}$ and time of concentration $t_c$, predictions frequently used in engineering hydrologic design and analysis.

KEYWORDS
analytical, contour-average, hillslope, hydrograph, kinematic wave, laboratory, ParFlow, runoff

## 1 | INTRODUCTION

Accurate prediction of overland flow processes is essential to a range of management challenges, including flash flooding (Bracken & Croke, 2007; Foody, Ghoneim, & Arnell, 2004), urban stormwater system management (Poff et al., 1997), and fluvial erosion (Howard, Dietrich, & Seidl, 1994). These outcomes impact infrastructure planning, design, flood risk estimation, and erosion mitigation (Grimaldi & Petroselli, 2015). Consequently, peak flow estimation for overland flow dominated systems has a long history, and numerous predictive methods are available to practitioners. These methods vary in their complexity, from numerical solutions of two-dimensional flow equations (Ashby & Falgout, 1996; Jones & Woodward, 2001; Kollet & Maxwell, 2006; Maxwell, 2013), to analytical expressions obtained from solutions of one-dimensional kinematic wave equations on a plane (Brutsaert, 2005), to even simpler empirical approaches such as the Rational Method (Kuichling, 1889; Mulvaney, 1851). Broadly, hydrologists selecting from these methods are faced with a tradeoff between process fidelity and ease of use, with the latter being particularly important for widespread adoption by practitioners (Douglas, 1991).

If ease-of-use is an important determinant of the uptake of a method, then improving the predictions made by simple methods, without making them significantly harder to use, would be particularly valuable. Opportunities for such improvement could be associated with making better use of information about the land surface that regulates flow, for example by incorporating data from remote sensing (Petroselli, 2012); or by increasing the physical basis of predictive tools (Grimaldi, Petroselli, Tauro, & Porfiri, 2012; Manoj et al., 2013).

The hillslope response has been studied extensively on rectangular hillslopes, primarily using the non-linear storage model (SM) (Agnese, Baiamonte, & Corrao, 2001; Baiamonte & Agnese, 2016) and the kinematic wave model (KWE) (Baiamonte & Singh, 2016a). These formulations have led to analytical formulae for calculating the time to equilibrium $t_e$ [T] and peak flow $Q_{peak}$ [$L^3$/T] of the hydrograph. Such kinematic wave solutions have been used to develop simplified peak flow prediction tools that incorporate the effects of infiltration (Baiamonte, 2020; Baiamonte & Singh, 2017). Here, we attempt to enable both analytical improvement and expansion of data use by extending solutions of the physically-based hillslope kinematic wave equation to account for surface topographic curvature, a land surface property that can be derived from lidar remote sensing. For sufficiently simple hillslope morphologies (compare Troch, van Loon, & Hilberts, 2004), the resulting solutions are analytical and represent only a modest increase in numerical complexity relative to existing formulae.

As outlined in Section 2, the major assumption needed to develop these predictions is that the two-dimensional flow field that arises on curved landscapes can be approximated by a one dimensional, contour-averaged value (Fan & Bras, 1998). Testing this assumption is challenging: two dimensional analytical solutions do not exist for the case at hand, and two-dimensional numerical models contain their own uncertainty (e.g., from numerical approximation). Similarly, although empirical observations of flow behavior are available, it is often not possible to simultaneously (a) constrain landscape curvature, (b) characterize the runoff generation process, and (c) obtain high-resolution, local rainfall data in the same landscape—all of which are needed for model testing. In this situation, laboratory-scale experiments have a useful role to play (Blume, van Meerveld, & Weiler, 2010; Kleinhans, Bierkens, & van der Perk, 2010). We therefore undertake experiments in which simulated rainfall is applied to scale-models of hillslopes with prescribed curvature and runoff generation mechanisms to generate datasets against which to test the analytical solution. Comparing the analytical solution against both numerical and experimental datasets controls for different kinds of errors, and increases our confidence in the performance of the solution.

## 2 | THEORETICAL DEVELOPMENT

### 2.1 | Background

The kinematic wave approximation simplifies the flow momentum equations under the assumption of steady, uniform flow when gravitational forces accelerating flow are balanced by a friction slope that parameterizes bed shear stresses. A history of kinematic wave modeling can be found in Baiamonte and Singh (2016a). The mass balance for flow along a trapezoidal two-dimensional cross-section is given by:

$$\frac{\partial H}{\partial t} + \frac{\partial Q}{\partial x} = (I - f)w \tag{1}$$

where $H$ is the flow cross-section [$L^2$]; $Q$ total flow across the cross-section [$L^3$/T]; $I$ rainfall intensity [L/T]; $f(x, t)$ infiltration rate [L/T]; $w(x)$ the width of the cross-section [L]; and $t$ [T] and $x$ [L] are the time and path coordinates respectively (Brutsaert, 2005). In general, for a cross-slope $y$ coordinate with $w = y_2 - y_1$,

$$H = \int_{y_1}^{y_2} h dy = w\bar{h} \tag{2}$$

where $h(x, y, t)$ is water depth [L] and $\bar{h}(x,t)$ is the average depth [L] along the cross-section, and

$$Q = \int_{y_1}^{y_2} q dy = w\bar{q} \tag{3}$$

where $q(x, y, t)$ is flow rate [$L^2$/T], and $\bar{q}(x,t)$ is the average flow [$L^2$/T] along the cross-section. Using Equations (2) and (3), we rewrite Equation (1) as:

$$\frac{\partial}{\partial t}\bar{h}w + \frac{\partial}{\partial x}\bar{q}w = (I - f)w. \tag{4}$$

In effect, this simplifies the equations to one dimension so that no terms depend on the cross-slope coordinate. The limitations of this approach are explored later. This one-dimensional averaged equation is equivalent in form to the solution for a one-dimensional streamline in the case of $w$ = *Const*. Note that overbars are omitted in this section since the results are applicable to both the one-dimensional equation and the contour averaged one-dimensional equation (Equation (4)) that represents two-dimensional flow. This approach is similar to Agnese, Baiamonte, and Corrao (2007), who employ a shape factor to solve the kinematic wave equation on a trapezoidal hillslope.

To solve these equations, the friction slope must be related to surface roughness and flow properties, typically via a Darcy-Weisbach friction factor. For turbulent flow, where the friction factor scales with relative roughness, this results in relationships between flow and depth of the form:

$$q = \alpha h^m, \tag{5}$$

which are often referred to as kinematic roughness equations (Brutsaert, 2005). The term $\alpha$ [$L^{2-m}$/T] depends on surface roughness, while $m$ depends on the flow regime. Units of $\alpha$ depend on $m$ in order to maintain homogeneous units. Here we use either $m$ = 5/3 or $m$ = 2 (Morgali, 1970; Woolhiser & Liggett, 1967), corresponding to turbulent or transitional flows respectively. $m$ = 3 corresponds to laminar flow, which is not considered in this study since overland flow is unlikely to be laminar.

The kinematic wave equation can be used to describe runoff generation during rainfall on a homogeneous hillslope. Runoff is generated homogeneously along the hillslope beginning at the time of ponding $t_p$, prior to which all rainfall infiltrates, and the flow depth is $h = 0$ by definition. A boundary condition of $h = 0$ is usually assumed at the hillslope divide ($x = 0$), which results in a no flow boundary condition for Equation (5). An initial water depth of $h = 0$ is assumed at all locations at $t = 0$ (Giráldez & Woolhiser, 1996). Kinematic flow that results from these conditions can be visualized via a *characteristic net*, as shown in Figure A1. Lines in the characteristic net represent space–time trajectories along which the flow equations can be simplified into ordinary differential equations. These trajectories are called the characteristics $t(x)$ of the wave equation (Lighthill & Whitham, 1955). Flow obeying the kinematic wave equation moves along the characteristics prescribed by $t(x)$ with depth ($h(x, t)$) and flow rate per unit contour width ($q(x, t)$). Hydrographs are generated by solving for flow at the hillslope outlet ($q(L, t)$), located at $x = L$. We generalize the concept of an outlet so that for a hillslope, the outlet refers not to a point of discharge but to the bottom boundary of the hillslope, which produces flow out of the landscape. The discharge $q$ is related to the flow celerity by Equation (5). The wave celerity $u$ is defined by $u = \frac{\partial x}{\partial t}$ $[L/T]$. As a characteristic becomes flatter ($\frac{\partial x}{\partial t}$ approaches $\infty$), the wave celerity $u$, depth $h$ (by Equation (7)), and therefore the flow per unit width $q$ (by Equation (5)) all increase.

Three distinct domains in the hydrograph—Domain 1—the rising limb, Domain 2—equilibrium flow, and Domain 3—the recession (or falling limb)—can be interpreted directly via the characteristic net. The hydrograph's rising limb is generated by characteristics originating at the time of ponding, anywhere in space (i.e., along the x-axis of the net). The further the origin of the characteristic from the outlet (the smaller $x$ at $t = t_p$) the later the characteristic crosses $x = L$; in other words, the contributing area of the hillslope increases over time until the characteristic originating at $x = 0$ (shown in solid gray) crosses $x = L$. At this time ($t = t_e$), the hillslope reaches an equilibrium flow condition, and the rising limb ends. For $t > t_e$, new characteristics can only be initiated at the divide, $x = 0$. On a planar hillslope experiencing constant $I$ and $f$, these characteristics behave identically until the end of the storm, leading to equilibrium (steady state) flow at $x = L$. When the storm ends at $t = t_r$, ponded water infiltrates without replenishment, slowing the flow and curving the characteristics upward. The fraction of these characteristics that cross the $x = L$ boundary form the falling limb of the hydrograph. The remainder describe the pathways taken by water that infiltrates on the hillslope. Solving the ordinary differential equations along the characteristics of the wave equation in these three domains results in three equations to describe a hydrograph: a solution structure we follow when considering convergent/divergent slopes.

## 2.2 | General equation

Equation (4) describes the average flow along a hillslope contour. Using $\bar{h}$ and $\bar{q}$ allow us to retain the simplicity of a one-dimensional equation but generalize solutions to non-planar hillslopes by defining the width function $w(x)$ that describes the linear distance between contour endpoints at each point $x$ along a hillslope. Here, we present solutions for the simplest case where rainfall with constant intensity $I$ falls on an impermeable slope with $f = 0$. The solution is unchanged for constant $f$, and can be generalized using, for example, the methods of Giráldez and Woolhiser (1996) for time-varying infiltration.

Using Equation (5), Equation (4) can be rewritten as:

$$\frac{\partial \bar{h}}{\partial t} + m\bar{h}^{m-1}\alpha\frac{\partial \bar{h}}{\partial x} = I - \alpha\frac{1}{w}\frac{dw}{dx}\bar{h}^m. \tag{6}$$

We use the method of characteristics (Lighthill & Whitham, 1955) to transform Equation (6) into a system of ODEs:

$$\frac{dx}{dt} = m\bar{h}^{m-1}\alpha \tag{7}$$

and

$$\frac{d\bar{h}}{dt} = I - \alpha\frac{1}{w}\frac{dw}{dx}\bar{h}^m. \tag{8}$$

## 2.3 | Analytical solutions

To obtain analytical solutions to Equation (8), we use an exponential width function with the form:

$$w(x) = ce^{ax}. \tag{9}$$

The exponential allows for both convergent ($a < 0$) and divergent ($a > 0$) slopes. The bottom row of Figure A1 illustrates the shape of hillslopes with an exponential width function for different values of $a$.

To proceed with a solution, we firstly we note that:

$$\frac{dw}{dx} = ace^{ax}, \tag{10}$$

allowing solution to Equation (8) through the simplified form:

$$\frac{d\bar{h}}{dt} = I - \alpha a\bar{h}^m. \tag{11}$$

To facilitate an analytical solution, we specify $m = 2$ in Equation (5) for mixed turbulent and laminar conditions. Semi-analytical solutions are available for other values of $m$ using a hypergeometric function. While we principally select $m = 2$ to preserve analytical tractability, this approximation is nonetheless reasonable for describing flow on most land surfaces (Baiamonte & Singh, 2015; Giráldez & Woolhiser, 1996).

With these assumptions, we separately solve the equations within the three space–time domains described in Section 2. Each domain corresponds to a different set of boundary conditions, for which Equations (7) and (11) are solved. To assist in navigating the equations, a list of symbols is provided as Table A1.

***Domain 1, the Rising Limb: Characteristics originating from*** $0 \le x \le L$, $t = t_p$

Characteristics in Domain 1 originate at the time of ponding at any point in space. The boundary conditions on these characteristics are $x = x_0$, where $x_0$ lies between the divide and the hillslope outlet, and $t = t_p$.

Equation (11) can be integrated subject to these boundary conditions:

$$\int_{t_p}^{t} dt = \int_0^{\bar{h}} \frac{1}{I - \alpha a \bar{h}^m} d\bar{h}, \tag{12}$$

yielding the semi-analytical equation:

$$t = t_p + \frac{\bar{h}}{I}\,{}_2F_1\left[1, \frac{1}{m}, 1 + \frac{1}{m}, \frac{a\alpha \bar{h}^m}{I}\right]. \tag{13}$$

where ${}_2F_1$ is the Gauss hypergeometric function (Abramowitz & Stegun, 1972). For $m = 2$, Equation (13) yields a relationship between the rainfall and hillslope properties ($f$ and $a$), time, and the depth of flow:

$$t = \begin{cases} t_p + \sqrt{\dfrac{1}{a\alpha I}}\tanh^{-1}\left(\bar{h}\sqrt{\dfrac{a\alpha}{I}}\right) & a \ge 0 \\ t_p + \sqrt{\dfrac{1}{-a\alpha I}}\tan^{-1}\left(\bar{h}\sqrt{\dfrac{-a\alpha}{I}}\right) & a \le 0 \end{cases} \tag{14}$$

The *tanh* function also appears in the expression for $q$ in solutions to the non-linear storage model when $m = 2$ (Agnese et al., 2001). We also integrate the other differential equation, Equation (7), with the boundary condition $x = x_0$ at $t = t_p$, and use Equation (11) to change the integration variable from $t$ to $h$:

$$\int_{x_0}^{x} dx = \int_{t_p}^{t} m\bar{h}^{m-1}\alpha dt = \int_0^{\bar{h}} \frac{\alpha m \bar{h}^{m-1}}{I - \alpha a \bar{h}^m} d\bar{h}, \tag{15}$$

giving:

$$x = x_0 + \frac{\ln(I)}{a} - \frac{\ln\left(I - a\alpha \bar{h}^m\right)}{a}, \tag{16}$$

Equation (16) can be re-arranged to express $\bar{h}$ as a function of $x$ and $x_0$:

$$\bar{h}(x) = \left(\frac{I - Ie^{ax_0 - ax}}{a\alpha}\right)^{1/m} \tag{17}$$

Substituting Equation (17) into Equation (13) gives the equation of the characteristics $t(x)$. Equation (17) is applied along the characteristics, giving $\bar{h}(x)$ for all initial conditions $x_0$. The depth of the flow at the hillslope outlet is given by $\bar{h}(L)$, which is substituted into Equation (5) to obtain the hydrograph.

For short storms (or for low wave celerities), the end of the storm $t = t_r$ may arrive before a characteristic reaches the hillslope outlet. In this case, the values $x$ and $\bar{h}$ at $t = t_r$ are noted as $x_*$ and $\bar{h}_*$ and provide the boundary conditions for the characteristics in Domain 3.

***Domain 2, Equilibrium Flow: Characteristics originating from*** $x = 0$, $t_p \le t \le t_r$

Characteristics in this domain originate at the hillslope divide between the time of ponding and the end of rainfall at $t = t_r$. The boundary conditions for the equation are $x = 0$ and $t_p \le t_0 \le t_r$. The relationship between time and flow depth along the characteristics is obtained by integrating Equation (11) from $t = t_0$ to $t$ (if the characteristic reaches $x = L$ by time $t$), or from $t = t_0$ to $t_r$ (for characteristics present on the domain at the end of rainfall):

$$\int_{t_0}^{t} dt = \int_0^{\bar{h}} \frac{1}{I - \alpha a \bar{h}^m} d\bar{h}, \tag{18}$$

which gives:

$$t = t_0 + \frac{\bar{h}}{I}\,{}_2F_1\left[1, \frac{1}{m}, 1 + \frac{1}{m}, \frac{a\alpha \bar{h}^m}{I}\right], \tag{19}$$

and again is fully analytical for $m = 2$:

$$t = \begin{cases} t_0 + \sqrt{\dfrac{1}{a\alpha I}}\tanh^{-1}\left(\bar{h}\sqrt{\dfrac{a\alpha}{I}}\right) & a \ge 0 \\ t_0 + \sqrt{\dfrac{1}{-a\alpha I}}\tan^{-1}\left(\bar{h}\sqrt{\dfrac{-a\alpha}{I}}\right) & a \le 0. \end{cases} \tag{20}$$

To obtain the characteristic equation, $x(t)$, Equation (7) is integrated for characteristics starting at $x = 0$, again using Equation (11) to change the variable of integration:

$$\int_0^{x} dx = \int_{t_p}^{t_0} m\bar{h}^{m-1}\alpha dt = \int_0^{\bar{h}} \frac{\alpha m \bar{h}^{m-1}}{I - \alpha a \bar{h}^m} d\bar{h}, \tag{21}$$

giving:

$$x = \frac{\ln(I)}{a} - \frac{\ln\left(I - a\alpha \bar{h}^m\right)}{a}. \tag{22}$$

The flow depth $\bar{h}$ can then be explicitly expressed as a function of $x$:

$$\bar{h}(x) = \left(\frac{I - Ie^{-ax}}{a\alpha}\right)^{1/m}. \tag{23}$$

When rain stops at $t = t_r$, values of $x$ and $\bar{h}$ on each characteristic, denoted as $x_*$ and $\bar{h}_*$, provide the initial conditions for Domain 3.

*Domain 3, the Recession/Falling Limb: Characteristics present on the hillslope at $t = t_r$ for all values of x along the hillslope until the time when no water remains on the surface*

For $t > t_r$, the rainfall rate $I = 0$, so Equation (11) becomes:

$$\frac{d\bar{h}}{dt} = -\alpha a \bar{h}^m. \tag{24}$$

All characteristics present in this domain originated from domains 1 or 2, and have boundary conditions $x_*$ and $\bar{h}_*$ at $t = t_r$ set by the solution from the previous domains. Integrating Equation (24) with these boundary conditions:

$$\int_{t_r}^{t} dt = \int_{\bar{h}_*}^{\bar{h}} \frac{-1}{\alpha a \bar{h}^m} d\bar{h}, \tag{25}$$

gives:

$$t = t_r + \frac{1}{a\alpha(m-1)}\left(\frac{1}{\bar{h}^{m-1}} - \frac{1}{\bar{h}_*^{m-1}}\right), \tag{26}$$

or in the case of $m = 2$,

$$t = t_r + \frac{1}{a\alpha}\left(\frac{1}{\bar{h}} - \frac{1}{\bar{h}_*}\right) \tag{27}$$

Equation (7) is then integrated, changing the variable of integration with Equation (24):

$$\int_{x_*}^{x} dx = \int_{t_r}^{t} m\bar{h}^{m-1}\alpha dt = \int_{\bar{h}_*}^{\bar{h}} -\frac{\alpha m \bar{h}^{m-1}}{\alpha a \bar{h}^m} d\bar{h} = \int_{\bar{h}_*}^{\bar{h}} -\frac{m}{a\bar{h}} d\bar{h}, \tag{28}$$

to give:

$$x = x_* + \frac{m}{a} ln\left(\frac{\bar{h}_*}{\bar{h}}\right). \tag{29}$$

And the flow depth $\bar{h}$ is then expressed as:

$$\bar{h} = \bar{h}_* e^{-\frac{a}{m}(x - x_*)}, \tag{30}$$

which can be solved for $x = L$ and converted from flow depth to discharge to obtain the hydrograph.

Thus, for constant $f$ and $I$, a set of general and numerically solvable solutions for any $m > 0$ are given by: Domain 1—Equations (13) and (23), Domain 2—Equations (19) and (23), and Domain 3—Equations (26) and (30). For the fully analytical solutions associated with $m = 2$ the relevant equations are: Domain 1—Equations (14) and (23), Domain 2—Equations (20) and (23), and Domain 3—Equations (27) and (30), in conjunction with Equation (5), used to relate flow depth $h$ to unit discharge $q$. A similar solution for trapezoidal hillslopes was presented by (Agnese et al., 2007).

## 2.4 | Modeling scenarios

We used the analytical model to explore the impact of hillslope divergence and convergence on hillslope hydrology. Firstly, we qualitatively explored the behavior of equilibrium and non-equilibrium storms on hillslopes with convergent versus divergent topography, and interpreted the behavior of the resulting characteristic nets and hydrographs in terms of hillslope topography. Next, to allow quantitative comparisons between hydrographs, we held the total hillslope area $A_{max}$ and length $L$ constant for three curvature cases: (a) a very convergent hillslope with $a = -0.02$, (b) a uniform width hillslope, described by $a = 0$, and (c) a very divergent hillslope with $a = 0.02$. We examined how the hydrograph shape, time to equilibrium flow $t_e$, and maximum discharge rate $q_{peak}$ for equilibrium storms ($t_r > t_e$, where the hydrograph demonstrates a period of constant equilibrium flow at the peak value) and non-equilibrium storms ($t_r \leq t_e$, where the peak is represented by a point, not an interval of equilibrium flow) varied as a function of the curvature parameter $a$.

The characteristic nets in Figure A1 show the model predictions for a non-equilibrium storm ($t_r > t_e$) and an equilibrium storm ($t_r \leq t_e$), and for convergent, planar, and divergent slopes. Different qualitative hydrograph behavior between the convergent and divergent slopes for an equilibrium storm is shown in the top row in Figure A1. The convergent hydrograph rises rapidly before reaching peak flow, whereas the divergent hydrograph rises in a more linear fashion from the start of the storm. These differences are intuitively related to the hillslope geometry of the different slopes, which means that the rate of change of *contributing* area, $\partial A/\partial t$, increases with time up to $t = t_e$ on convergent slopes, but declines on divergent slopes.

The shape of the characteristics differs between the convergent and divergent cases. For the convergent slope, the characteristics become flatter with increasing $x$, indicating acceleration of the flow as it is concentrated by the slope convergence.

The characteristics on the divergent slope approach a constant velocity (a diagonal line on the characteristic net) as $x$ increases. After the storm ends, the flow on the convergent slope continues to accelerate as it exits the domain. On the divergent slope, the curvature decelerates the flow, causing a rapid recession.

Non-equilibrium storm conditions are shown in the middle row of Figure A1. In these storms, the boundary characteristics originating from $x = 0$ (shown in dark gray) do not reach the bottom of the hillslopes before the storm ends. On the convergent hillslope, the hydrograph continues to rise after the non-equilibrium storm ends. This reflects the large volume of water already present in the domain at the upslope end of the watershed, and its acceleration downslope via topographic convergence, evident in the flattening of the characteristics even after the rain ends at $t_r$. Even though the boundary characteristic crosses the outlet well after $t_r$, it is the crossing of this characteristic that determines the timing of the peak flow (compare with a planar slope for non-equilibrium storms, where peak flow corresponds to the end of the storm (Giráldez & Woolhiser, 1996)). For the divergent hillslope, the end of the non-equilibrium storm coincides with $q_{peak}$. Like the equilibrium storm case, the water on the hillslope decelerates due to topographic divergence, infiltrates locally, and forms a steep falling limb.

Figure A2 shows the hydrographs produced by three exponential width hillslopes of equal area but different curvature (very convergent $a = -0.02$, uniform width $a = 0$, and very divergent $a = 0.02$) for a 60 min duration, 5 cm/hr storm with no infiltration. All hillslopes reach equilibrium. The divergent slope (dark blue) hydrograph rises fastest initially, since most of the hillslope area is close to the outlet. The convergent slope hydrograph rises sharply as the runoff from higher in the watershed reaches the outlet, since most of the watershed area is far from the outlet. Thus, the approach to $q_{peak}$ is gentle for the divergent slope hydrograph and becomes sharper as the slope becomes more convergent. All slopes exhibit the same total maximum flow $Q_{peak}$, but the convergent slope produces this maximum first. As seen in Figure A2, the difference in the time of equilibrium $t_e$ is more than 20% between the slopes.

Unsurprisingly, the degree and directionality of curvature has a direct impact on the peak flow per unit contour $q_{peak}$ at the hillslope outlet, as shown in the inset in Figure A2. While all hillslopes produce the same total hillslope discharge, due to the equilibrium conditions, and identical hillslope area and storm properties, the unit discharge is normalized by contour length, generating the different values of $q_{peak}$. While trivial, this result is also linked to large differences in flow depth and velocity with differences in curvature, with important practical outcomes for, for example, inundation, erosion risk and safety.

The divergent slope hydrograph falls most steeply during the recession, reflecting that most water on the hillslope at the end of the storm is located near the outlet. Flow from the uniform width and convergent slopes declines more slowly.

## 3 | METHODS

### 3.1 | Comparison to numerical simulations

The analytical solutions obtained above required several assumptions, notably the assumption that flow is one-dimensional along lines of steepest descent (streamlines), and that the flow is near-uniform along contours. For sufficiently curved slopes, the two-dimensional nature of surface flow would violate these assumptions, making the analytical solutions unreliable. To identify when this occurs, we compared predictions of the hillslope hydrograph made with the solutions obtained in Section 2 to predictions made using numerical solutions of the two-dimensional kinematic wave equations on a common set of divergent and convergent hillslopes. We used ParFlow (Ashby & Falgout, 1996; Jones & Woodward, 2001; Kollet & Maxwell, 2006; Maxwell, 2013) to solve the two-dimensional kinematic wave equations for a range of values of $a$. ParFlow represents flow resistance using Manning's equation. We therefore firstly compared ParFlow output to numerical solutions of our semi-analytical $m = 5/3$ solution. We also compared the ParFlow predictions to the analytical solutions where $m = 2$, noting that in these cases, error arises from both the change in the value of $m$ between ParFlow and the solution, and from loss of validity of the assumptions. To evaluate the similarity between ParFlow and our solutions, we compared the peak discharge, the RMSE between the numerical hydrographs and the (semi-)analytical hydrographs, and the difference between hydrograph shapes, which we evaluated with a metric $\xi$, defined as the RMSE between two hydrographs, normalized by the maximum flow rate. If the assumptions used in the derivation are met, then peak flows would be identical on identical hillslopes simulated by the different models, and the RMSE and the shape metric $\xi$ would tend to zero. We also report the coefficient of variation (CV) in flow across all hillslope cells at the outlet in the ParFlow simulation as a metric of uniformity across the contours, anticipating that the analytical solutions would become less reliable as CV increased. Several ParFlow simulations on divergent hillslopes formed a localized numerical instability around the center-line of the domain. Although persistent, the instability represented <0.01% of the flow. We removed these aberrant points and interpolated the flow predictions across the gap before comparing to the analytical solutions.

We compared analytical and ParFlow solutions for a range of hillslopes with exponential width functions produced with the equation suggested by Evans (1980):

$$z = E(1-x/L)^k + \omega y^2, \tag{31}$$

where $x$ and $L$ are again the hillslope coordinate and the hillslope length; $y$ is the cross-slope horizontal coordinate, with $y = 0$ corresponding to the centre-line of a symmetrical hillslope; $z$ is vertical elevation above a datum located at $x = L$; $E$ is the elevation change between $x = 0$ and $x = L$ at $y = 0$; and $k$ and $\omega$ are parameters describing hillslope curvature. Examples of this topography are shown in Figure A1.

The lines of steepest descent are given, for $k = 1$, by:

$$y = \frac{C}{2} e^{-\frac{2\omega L}{E}x}, \tag{32}$$

where $C/2$ is a constant of proportionality. For flow that follows the lines of steepest descent, we can truncate the landscape along any streamline without altering flow behavior in the remaining section of the landscape.

To do this, we define a hillslope that is symmetric about $y$=0, with width function:

$$w = 2\frac{C}{2} e^{-\frac{2\omega L}{E}x} or \tag{33}$$

$$w = Ce^{ax}, \tag{34}$$

where $a = -2\omega L/E$.

The expression for $a$ shows that for $\omega > 0$, the hillslope is convergent, and for $\omega < 0$, the hillslope is divergent. Values of $C$ were computed by fixing $L$, $E$, $\omega$ and a hillslope area $A_{max}$ across all simulations.

We generated landscapes with $a$ values ranging from $a = -0.1$ to $a = 0.1$ on a hillslope with $E = 2.5$ m and $L = 50$ m, holding the hillslope area constant for all simulations. We ran all simulations with Manning's $n = 0.0001$ during a 125 min rainstorm with 50 mm/hr intensity. While the Manning's $n$ used in these simulations is unusually small and not likely to represent real landscapes, sensitivity tests indicate that qualitative results are insensitive to the choice of $n$, and a small $n$ value allows us to resolve the full falling limb with decreased computational cost. We checked that ParFlow simulations were stable with respect to a change in space or time discretization (see Appendix I). All simulations were therefore run using $\Delta x = 0.5$ m and $\Delta t = 0.005hr$.

## 3.2 | Experimental

### 3.2.1 | Model set-up

Three model hillslopes were constructed using CNC machining to conform to Equation (31), for three values of $a$: a convergent hillslope with $a = -0.05$, a planar hillslope with $a = 0$, and a divergent hillslope with $a = 0.05$. A script used to produce 3-D printed prototypes is included in the data supplement (Lapides, David, Sytsma, Dralle, & Thompson, 2020). Models were built at scale so that for $a = -0.05$, spatial measurements scale at 1:30 compared to full-scale, and $a = 0.05$ is constructed at 1:40 scale. The $a = 0$ hillslope can be considered at any scale, allowing for easy comparison to both the $a = 0.05$ and $a = -0.05$ hillslope cases. The particular scaling is explicitly required since the width function is exponential with distance. For instance, if the outlet is 1 m wide, and the divide is 0.2 m wide for a hillslope that is 1 m long, the optimal exponential fit is $w = 0.2e^{1.61x}$. If we consider this to be a 1:100 scale model, then the best fit is $w = 20e^{0.0161x}$m. Thus, both $C$ and $a$ scale with the scaling parameter, so the scale controls the value of $a$. Thus, the scale and value of $a$ must be chosen together. Considering the slope at a different scale changes the value of $a$. Hydrodynamic scaling considerations, which are also important, are described later in Section 3.

The hillslopes were constructed from 1 m × 1 m × 0.025 m insulation foam blocks, glued together with marine grade epoxy to form an initial 0.08 m high blank. CNC machining of these blanks is shown in Figure A3 (a) and (b). Following machining, the hillslope surfaces were smoothed by filling cracks with insulation foam and marine grade epoxy, and the filled cracks were sanded to match the adjacent surface height using 0.5 mm sandpaper, leaving the finish shown in Figure A3 (c). This finished surface was hydrophobic, so we coated the hillslopes with <250$\mu$m sieved builders sand at a average density of 0.22 g/cm$^2$ (based on the weight of sand applied to the known hillslope areas), using a thin layer of epoxy as an adhesive. The resulting final surfaces of the hillslopes are shown in Figure A3 (d) for $a = -0.05$, (e) for $a = 0$, and (f) for $a = 0.05$. Finally, we used aluminium foil to form boundary conditions and prevent water entering or leaving the model hillslope domain.

We constructed a simple rainfall simulator by arranging 6 atomizing nozzles pointing directly down at locations shown in Figure A4. Nozzles were connected to a University of California Berkeley building water main via a valve with a pressure equalizer. The path to each nozzle from the valve was of an equivalent length and passed through through identically sized tubes and connectors. We restricted the outlets to 6 nozzles in order to maintain high enough pressure in the system to achieve atomizing spray. If pressure drops, nozzles drip intermittently, creating large changes in uniformity of the rainfall. Tests of the rainfall simulator performance showed that it was variable (average coefficient of uniformity of 17% compared to benchmarks of 70–94% Humphry, Daniel, Edwards, & Sharpley, 2002; Esteves, Planchon, Lapetite, Silvera, & Cadet, 2000; Moore, Hirschi, & Barfield, 1983; Shelton, von Bernuth, & Rajbhandari, 1985; Meyer & Harmon, 1979), and that some areas received systematically more rainfall than others (see Appendix Section II for details of the tests). However, this spatial pattern was symmetrical and persistent across tests. While the simplicity of the simulator design means that effective rainfall on hillslope scales needs to be back-calculated from equilibrium flow values, the performance of the rainfall simulator was robust enough for us to proceed with flow generation experiments.

The experiment was set up as shown in Figure A4 (b). Hillslope models were placed on a levelled surface, with the rainfall simulator 0.7 m above the model. A funnel constructed of medium density fiberboard and aluminium foil was used to direct flow from the base of the hillslope into a beaker on a mass balance. Rainfall was initiated while the hillslope was covered with an impermeable cover. Once the cover was removed, we subjected the hillslopes to 5 or 10 min of rainfall simulation, after which the rain cover was replaced (and the simulator turned off), and flow continued until it became negligible. The mass of the beaker was recorded continuously throughout each experiment and tabulated on one-second intervals. Experiments were run 3–5 times for each hillslope.

We smoothed mass-time curves by quadratic locally-weighted regression with a tricubic kernel using the python statsmodels library (Cleveland, 1979; Hastie, Tibshirani, & Friedman, 2009). An optimal smoothing method was determined by selecting the method that produced the hydrograph with the smoothest curve that accurately fits the data. This was determined by examining the RMSE between the smoothed curve and the data in addition to the "noisiness" of the curve, measured as the mean frequency of concavity reversal. The resulting smoothed curve was converted into a hydrograph using a finite difference method. Details on quality control of hydrographs and the selection of an optimal smoothing method can be found in Appendix Section III. A list of the tested methods is found in Table A4.

To enable us to parameterize the constants in the experiment, we separately analyzed (a) the rising limb, (b) equilibrium peak flow, and (c) the falling limb of the hydrograph. Because the strongest sensitivity to curvature is found in the rising limb of the hydrograph, we used equilibrium peak flow to compute the effective rainfall intensity, and the falling limb to parameterize the roughness coefficient for the hillslopes.

With no infiltration occurring on the model hillslopes, rainfall intensity can be computed from equilibrium flow. Equilibrium flow was identified by taking the mean value of the top 10% of flow measurements (results are not sensitive to variations in these thresholds). With the equilibrium flow ($Q_{peak}$) defined, the effective hillslope-average rainfall rate was estimated as:

$$I = \frac{Q_{peak}}{A}, \tag{35}$$

Rainfall rates estimated using this procedure varied from 7–12 mm/hr. This compares well to the average flow rate measured at the nozzles which was ≈10 mm/hr (see Appendix Section II).

Once the effective rainfall rate was estimated, we calibrated the kinematic roughness parameter $\alpha$ by minimizing the RMSE between the observed falling limb of the hydrograph and the analytical solution for each experimental replicate and then averaging these values across all replicates. The falling limb was defined by all flow that occured following the recorded time of rainfall cessation.

We used the calibrated value of $\alpha$ to define the time to equilibrium $t_e$ and the the rising limb of the hydrograph for all simulations. We used the RMSE between the rising limb of the experimental hydrograph and the analytical prediction from the model, normalized by peak flow of the analytical hydrograph, (NRMSE) to measure how well the analytical solutions approximated the flow behavior. We examined the relationship between $t_e$ and curvature $a$ since $t_e$ is an important parameter for design. We also repeated the fit routine using analytical solutions with $a = 0$ to evaluate the reduction in prediction error achieved by incorporating curvature into the analytical solutions.

### 3.2.2 | Hydrodynamic scaling relationships

To enable the experimental models to provide a valid test of the theory, it is important to verify that the flow dynamics on the models are consistent with the assumptions used in the theory's derivation. This is a less rigorous constraint on the model design than the full dynamic similarity required for scale model construction in fluid mechanics/aerodynamics situations (Kundu, Cohen, & Hu, 2008), in which the value of the non-dimensional variables describing the flow must be conserved. Here it will be sufficient to confirm consistency with the two main assumptions used in deriving the theory: that (a) the flow is kinematic, and (b) the momentum equation can be approximated by a kinematic resistance formulation. These assumptions provoke consideration of three dimensionless numbers—the kinematic number

$$Ki = S_0 L / Fr_{0L}^2 h_{0L} \tag{36}$$

the Froude number ($Fr = u_{0L}/(gh_{0L})^{1/2}$) and the relative roughness ($rr = \varepsilon/h$). In these expressions, $S_0$ is the slope, $L$ the hillslope length, $h$ the flow depth, $u$ the flow velocity, $g$ gravitational acceleration, and $\varepsilon$ the characteristic lengthscale of roughness elements; the subscript $0L$ indicates the normal depth/velocity at location $x = L$—i.e., the hillslope outlet. We seek to verify that $Ki \gg 1$, meaning the use of the kinematic wave number is appropriate (Brutsaert, 2005, and references contained within), that $Fr \ll 1$, meaning flow is subcritical and stable and thus unlikely to change rapidly and violate the assumptions of normal flow required by the kinematic resistance formulation (White, 1999), and that the relative roughness is $\ll 1$, meaning that resistance to the flow is primarily produced by bed shear, rather than by distributed drag elements. We note, however, that distributed drag is also represented reasonably well by formulations that are mathematically equivalent to the kinematic roughness equations used here (see Crompton, Katul, & Thompson, 2020). We computed these dimensionless numbers for all hillslopes and verified that $Ki > 10{,}000$ in all cases, that $Fr < 0.12$ in all cases (with variations in $Fr$ across the hillslopes being less than one order of magnitude), and that $rr < 0.6$, at least for equilibrium flow conditions. During low flow conditions, $rr > 1$ likely occurs. However, because (a) we separately calibrate $\alpha$ for each experiment, (b) the form of the resistance equation is similar across all values of $rr$, and (c) the choice of roughness scheme is less important for producing the correct hydrograph during hillslope runoff than proper calibration of any selected scheme (Crompton et al., 2020), these variations are not problematic for the verification of the theory with the experimental hillslopes. All three conditions—$Ki \gg 1$, $Fr \ll 1$ and variable $rr$ that is nonetheless typically <1 for equilibrium flow, would apply to "full sized" hillslopes using typical estimates of rainfall, hillslope and land surface properties.

## 4 | RESULTS

### 4.1 | Numerical

Full data for the comparison between the analytical hydrographs (with $m = 2$ and $m = 5/3$) and the numerical solutions (via ParFlow) are presented in the Appendix Section 7, collected in Table 2. All forms of error remain relatively small until $|a| \geq 0.02$. At this point, the magnitude of error in the hydrograph increased in a stepwise fashion. Given these large increases in error, we considered the range $|a| \leq 0.02$ to represent the "reasonable" range of application for the analytical model, for both $m = 2$ and $m = 5/3$. Since results were qualitatively similar for both values of $m$, only results for $m = 5/3$ are shown. Quantitative values differ between the two sets of numerical simulations, with always greater error for the $m = 2$ simulations (see Table A2), due to the added error in the mismatch between the value of $m$ in numerical and analytical simulations. Note that the experimental studies use $|a|$ values of 0.05, outside the boundaries of the reasonable range defined by numerical simulations, which were selected in order to maximize the effects of curvature on the flow and examine whether the limitations of the model may appear different when examined with laboratory methods.

Within the reasonable range of $a$, the error metrics $\xi$ and RMSE remain fairly small. Figure A5 (a) shows how $\xi$ varies with $a$ as a proportion relative to $a = 0$. The RMSE is comparable to that of the $a = 0$ case (values similar to 1) when $|a| \leq 0.02$, but increases for larger $a$.

In Figure A5 (b), the proportional error in maximum flow is compared to the expected equilibrium condition of $A_{max} * I$. Errors in maximum flow increase with increasing $|a|$ when $a > 0$, and the value becomes larger for $a > 0.05$. While peak flow error decreases when $a < -0.02$, this decrease may be due to lower resolution data at the outlet since the number of cells at the outlet decreases as the hillslope becomes more convergent. Errors in the mean specific discharge across the boundary are less than 20% within the reasonable range. These errors are due to violation of the quasi-1D flow assumption. The lack of uniformity in flow across contours is illustrated by the coefficient of variation (CV) in the boundary flux shown in Figure A5 (c). The larger this CV, the less uniform the flow crossing the bottom boundary is. For divergent hillslopes ($a > 0$), CV remains relatively small since the tendency of the hillslope to disperse flow bounds the minimum specific discharge at 0. However, for convergent hillslopes ($a < 0$), the concentration of flow leads to effectively unbounded growth in peak specific discharge across the slope, leading to increasing CV as hillslopes become more convergent. The data point for $a = -0.10$ is plotted in grey, and violates this increasing trend: this is due to the resolution of the ParFlow simulation that results in very few boundary cells for the strongly convergent slope. The drivers of the increasing CV with increasing convergence are illustrated in Figure A5 (d), where the solid lines show the variations in specific discharge along the bottom boundary, which diverge further from the mean boundary discharge (dotted line) as $|a|$ increases.

## 4.2 | Experimental

The two hydrographs that meet quality standards for each of the hillslopes were used for comparison to analytical predictions. Figure A6 shows sample experimental and prediction hydrographs for (a) $a = -0.05$, (b) $a = 0$, and (c) $a = 0.05$. Parameterized roughness values are shown in Table A3. The effective rainfall rates are of the same order of magnitude, indicating that, while the rainfall is not spatially uniform, the hillslopes of different shapes received similar amounts of rainfall. It is visually apparent from the hydrographs in the upper half of the figure that shape of the rising limbs differs between curvature cases, with a steeper rising limb in the convergent case and a less extreme rising limb for the divergent case.

When normalized and plotted together in panel (d), the differences in the hydrographs due to curvature become more apparent. The divergent hydrograph contributes flow immediately and slowly increases, while the convergent hydrograph doesn't discharge much flow at first before rapidly rising to produce equilibrium peak flow. The result is that the time to equilibrium $t_e$ occurs sooner for the convergent than the divergent hillslope, as predicted by the analytical model. This trend is shown in panel (e). The values of $t_e$ for each hillslope are distinct, and there is a clear trend of increasing $t_e$ with increasing $a$.

The agreement between predicted and observed hydrographs is apparent from Figure A6 (a), (b), and (c) and reflected in the small NRMSE values for the curvature-included model referenced in panels (a)-(c) and plotted in panel (f) in blue for all hydrographs, while the NRMSE for the curvature-removed fit (orange) is at least an order of magnitude greater. This result indicates that including information about curvature improves the predictions of hydrographs formed on the experimental hillslopes, especially for divergent hillslopes, and suggests that even the simplified analytical solutions used in this study provide a very good approximation to the experimental results. It is notable that this agreement on the experimental hillslopes is better than expected, for the specific level of curvature, based on the ParFlow simulations. Potentially the reasonable range of $a$ selected using the ParFlow simulations ($|a| < 0.02$) is too conservative.

The value of $\alpha$ varied across the experimental hillslopes, a variation we attribute to heterogeneity in the application of the sand layer. If $\alpha$, rather than $a$, were the primary parameter controlling goodness-of-fit then the difference in NRMSE for the curvature-included and curvature-removed models in Figure A6 (f) would be minimal (as both models would have identical and calibrated $\alpha$ values). The significant difference in model performance associated with including information about $a$ in the predictions suggests that the variations in $\alpha$ reflect surface preparation rather than a parameterization of the effects of curvature.

# 5 | DISCUSSION AND CONCLUSION

This study extended the concept of hillslope width functions from groundwater flow (Fan & Bras, 1998; Troch, van Loon, & Hilberts, 2002) to surface runoff, predicting the hydrograph generated by uniform infiltration excess overland flow on convergent or divergent hillslopes, and allowing elegant analytical solutions for exponential hillslopes. Relative to existing techniques to simplify predictions for kinematic flow on topographically curved slopes, the present approach generates simpler and more intuitive predictions. Despite the approximation of the two-dimensional flow field with one-dimensional averaged flow needed to generate these solutions, predictions agreed well with both experimental observations and two-dimensional numerical predictions.

## 5.1 | Model applicability

The solution approach required the use of reasonably stringent assumptions, both around near one-dimensionality of flow, and around the imposition of exponential width-functions and use of an $m = 2$ exponent to allow analytical tractability. We note that previous experiments and analyses have found that $m = 2$ is often a reasonable approximation under transitional overland flow conditions (Henderson & Wooding, 1964; Thompson, Katul, Konings, & Ridolfi, 2011). Of course, with the exception of the one-dimensional approximation, these constraints can be relaxed, and simple numerical solutions for the one-dimensional flow problem can be used.

In approximating a conic section, a trapezoidal hillslope shape has been assumed in prior work (Agnese et al., 2007; Baiamonte &

Singh, 2016b), also derived for any value of $m$, including $m$ = 2 and $m$ = 5/3. An exponential hillslope shape was assumed by Troch et al. (2004). At present, GIS tools are available to simply delineate trapezoidal hillslope shapes (e.g., Noël, Rousseau, Paniconi, & Nadeau, 2014), and tools are under development by the authors for exponential forms. The generality of either morphology for describing real hillslopes is not well established, and each form has advantages—the simplicity of planar forms for a trapezoidal assumption, and the smoothness and continuity of exponential forms.

Where hillslopes exhibit very strong convergence or divergence (i.e., where $|a| > 0.02$), the assumption that flow occurs in a one dimensional sense along streamlines that follow the path of steepest descent may become invalid. On sufficiently curved hillslopes, water surface gradients arise that cause the flow vectors to deviate from the topographic path of steepest descent. Such flows are increasingly two-dimensional in their character, leading to increased variability in velocity and depth along hillslope contours. For such variable conditions the assumption that an average depth or velocity is a good representation for all flow conditions along the contour is inappropriate. This results in discrepancies between the analytical solution and two-dimensional numerical solutions to the flow equations, which tend to become more extreme as $|a|$ becomes larger.

The implications of this constraint, however, may be less problematic than it might appear at first sight. This is largely because the representation of overland flow as sheet flow via the kinematic wave equation is itself also constrained in its applicability—typically to hillslope scales on the order 100 s of meters. At this scale, numerous hillslopes fall within the curvature range where the solution is applicable, even in natural settings (Istanbulluoglu, Yetemen, Vivoni, Gutiérrez-Jurado, & Bras, 2008; Tarolli & Dalla Fontana, 2009). The restriction may be even less problematic in managed or anthropogenic settings such as urban landscapes, since these landscapes are often subject to deliberate grading and topographic control, which tends to reduce rather than exaggerate curvature. Thus, there are many situations where accounting for curvature via the solutions presented here could improve hydraulic predictions without exceeding the limits of validity of these solutions.

## 5.2 | Laboratory experimentation

The laboratory experiments provided a useful test of this method and complement the comparisons to numerical techniques. Because the sources of error in each approach (numerical versus experimental) are independent, the two comparisons provide a robust assessment of a new solution in a situation where two-dimensional analytical solutions were not readily available. While time-consuming and labor-intensive to construct and complete, the laboratory models allowed us to construct a highly controlled environment for testing, in which the only simplifications made relate to scale. In this situation, laboratory experiments filled a gap left between full-scale observations, which were not sufficiently controlled to allow testing of a new analytical solution, and numerical methods which also contained simplifications of physics and numerical errors, suggesting the value of augmenting existing hydrological methods with such laboratory approaches (Blume et al., 2010; Kleinhans et al., 2010).

The laboratory experiments also provide an opportunity to qualitatively assess the applicability of solutions developed for trapezoidal hillslopes by Agnese et al. (2007) and Baiamonte and Singh (2016b). Agnese et al. (2007) found that $t_e$ decreases with increasing divergence using the non-linear storage model, while Baiamonte and Singh (2016b) found that $t_e$ increases with increasing divergence using the kinematic wave model, similar to the solutions presented in this study. Experimental results definitively show a trend of increasing $t_e$ with increasing divergence, showing better agreement with the kinematic wave model than the storage model.

## 5.3 | Utility of methods

New technologies such as airborne and ground-based LiDAR, drone-based platforms, and micro-satellites have dramatically increased the ability of planners and hydrologists to observe the features of the landscapes they work in, especially as innovations increase the resolution and decrease the cost of obtaining information. Increasingly, planners and hydrologists confront the issue of how to use, rather than how to obtain such information. Techniques that can ingest this information without greatly increasing the demands on planners and engineers are appealing in this space. The analytical approach outlined in this study addresses these requirements, being simpler to execute and less computationally intensive than distributed numerical models, accurate within defined limits of reliability, and allowing predictions to become sensitive to features such as curvature. The theory is useful for calculating hydrographs from relatively small overland-flow dominated areas where flow convergence or divergence is expected. The physically-based nature of the theory makes it suitable for flow estimates where data needed to parameterize a more complex model are unavailable, or where ease-of-use or resource constraints require using simple tools.

The analytical solutions presented in this study provide a simple-to-execute method for predicting peak flow on topographically curved hillslopes. The joint verification of analytical solutions against numerical and experimental results provides a robust method for investigating the limitations of an analytical model under idealized conditions. This method could profitably be applied to other models to assess whether the assumptions truly hold in real systems, allowing for an exploration of whether models are truly "getting the right answers for the right reasons" (Kirchner, 2006).

**ACKNOWLEDGMENTS**

We would like to thank Michael Manga for generously providing lab space for the experiments conducted, Jeannie Wilkening for help in the lab, Twiggy Chen for assistance with 3-D printing and CNC fabrication, Erica Woodburn and Fadji Maina for guidance on setting up and running ParFlow, and Hana Moidu and Ellin Zhao for useful discussion. This work was supported by Engineering Research Center for

Reinventing the Nation's Urban Water Infrastructure (ReNUWIt) (AS), the National Science Foundation grants EAR-1013339 and EAR-BSF1632494 (DAL), the Hellman Foundation (DAL), the Gledden Foundation at the University of Western Australia's Institute for Advanced Studies (AS), the Undergraduate Research Apprenticeship Program (URAP) at University of California (CD), Berkeley, and the University of California, Berkeley (DAL).

## DATA AVAILABILITY STATEMENT

Data, models, and code generated during the study are available in a repository online (https://github.com/lapidesd/Hillslope_Storage_Kinematic_Wave), including programs for running the analytical and semi-analytical solutions, numerical data from ParFlow with a code for visualization, and experimental data with code to visualize, process, and compare results (Lapides et al., 2020b).

## ORCID

*Dana A. Lapides* https://orcid.org/0000-0003-3366-9686

## REFERENCES

Abramowitz, M., & Stegun, I. A. (Eds.). (1972). *Handbook of mathematical functions with formulas, graphs, and mathematical tables*, Washington, D.C.: . National Bureau of Standards Applied Mathematics Series 55.

Agnese, C., Baiamonte, G., & Corrao, C. (2001). A simple model of hillslope response for overland flow generation. *Hydrological Processes*, *15*(17), 3225–3238.

Agnese, C., Baiamonte, G., & Corrao, C. (2007). Overland flow generation on hillslopes of complex topography: analytical solutions. *Hydrological Processes: An International Journal*, *21*(10), 1308–1317.

Ashby, S. F., & Falgout, R. D. (1996). A parallel multigrid preconditioned conjugate gradient algorithm for groundwater flow simulations. *Nuclear Science and Engineering*, *124*(1), 145–159.

Baiamonte, G. (2020). A rational runoff coefficient for a revisited rational formula. *Hydrological Sciences Journal*, *65*(1), 112–126.

Baiamonte, G., & Agnese, C. (2016). Quick and slow components of the hydrologic response at the hillslope scale. *Journal of Irrigation and Drainage Engineering*, *142*(10), 04016038.

Baiamonte, G., & Singh, V. P. (2015). Overland flow times of concentration for hillslopes of complex topography. *Journal of Irrigation Drainage Engineering*, *3*, (3), 142.

Baiamonte, G., & Singh, V. P. (2016a). Analytical solution of kinematic wave time of concentration for overland flow under green-ampt infiltration. *Journal of Hydrologic Engineering*, *21*(3), 04015072.

Baiamonte, G., & Singh, V. P. (2016b). Overland flow times of concentration for hillslopes of complex topography. *Journal of Irrigation and Drainage Engineering*, *142*(3), 04015059.

Baiamonte, G., & Singh, V. P. (2017). Modeling the probability distribution of peak discharge for infiltrating hillslopes. *Water Resources Research*, *53*(7), 6018–6032.

Blume, T., van Meerveld, I., & Weiler, M. (2010). The role of experimental work in hydrological sciences – insights from a community survey. *Hydrology and Earth System Sciences*, *62*(3), 334–337.

Bracken, L. J., & Croke, J. (2007). The concept of hydrological connectivity and its contribution to understanding runoff-dominated geomorphic systems. *Hydrological Processes*, *21*(13), 1749–1763.

Brutsaert, W. (2005). *Hydrology: An introduction*, Cambridge, New York: . Cambridge University Press.

Cleveland, W. S. (1979). Robust locally weighted regression and smoothing scatterplots. *Journal of the American Statistical Association*, *74*(368), 829–836.

Crompton, O., Katul, G. G., & Thompson, S. (2020). Resistance formulations in shallow overland flow along a hillslope covered with patchy vegetation. *Water Resources Research*, *56*(5), e2020WR027194.

Douglas, J. L. (1991). Hydrology: Infusing science into a demand-driven art. In D. S. Bowles & P. E. O'Connell (Eds.), *Recent advances in the modeling of hydrologic systems* (pp. 31–43). Dordrecht, Netherlands: Kluwer Academic Publishers, Chapter 2.

Esteves, M., Planchon, O., Lapetite, J. M., Silvera, N., & Cadet, P. (2000). The 'EMIRE' large rainfall simulator: design and field testing. *Earth Surface Processes and Landforms*, *25*(7), 681–690.

Evans, I. S. (1980). An integrated system of terrain analysis and slope mapping. *Zeitschrift für Geomorphologie. Supplementband Stuttgart*, *36*, 274–295.

Fan, Y., & Bras, R. L. (1998). Analytical solutions to hillslope subsurfacestorm flow and saturation overland flow. *Water Resources Research*, *34*(4), 921–927.

Foody, G. M., Ghoneim, E. M., & Arnell, N. W. (2004). Predicting locations sensitive to flash flooding in an arid environment. *Journal of Hydrology*, *292*(1–4), 48–58.

Giráldez, J. V., & Woolhiser, D. A. (1996). Analytical integration of the kinematic equation for runoff on a plane under constant rainfall rate and Smith and Parlange infiltration. *Water Resources Research*, *32*(11), 3385–3389.

Grimaldi, S., & Petroselli, A. (2015). Do we still need the Rational Formula? An alternative empirical procedure for peak discharge estimation in small and ungauged basins. *Hydrological Sciences Journal – Journal des Sciences Hydrologiques*, *60*(1), 67–77.

Grimaldi, S., Petroselli, A., Tauro, F., & Porfiri, M. (2012). Time of concentration: a paradox in modern hydrology. *Hydrological Sciences Journal*, *57*(2), 217–228.

Hastie, T., Tibshirani, R., & Friedman, J. (2009). *The elements of statistical learning: Data mining, inference, and prediction*, New York: . Springer Science & Business Media.

Henderson, F. M., & Wooding, R. A. (1964). Overland flow and groundwater flow from a steady rainfall of finite duration. *Journal of Geophysical Research*, *69*(8), 1531–1540.

Howard, A. D., Dietrich, W. E., & Seidl, M. A. (1994). Modeling fluvial erosion on regional to continental scales. *Journal of Geophysical Research: Solid Earth*, *99*(B7), 13971–13986.

Humphry, J. B., Daniel, T. C., Edwards, D. R., & Sharpley, A. N. (2002). A portable rainfall simulator for plot-scale runoff studies. *Applied Engineering in Agriculture*, *18*(2), 199–204.

Istanbulluoglu, E., Yetemen, O., Vivoni, E. R., Gutiérrez-Jurado, H. A., & Bras, R. L. (2008). Eco-geomorphic implications of hillslope aspect: Inferences from analysis of landscape morphology in central new mexico. *Geophysical Research Letters*, *35*, L14403.

Jones, J. E., & Woodward, C. W. (2001). Newton–krylov-multigrid solvers for large-scale, highly heterogeneous, variably saturated flow problems. *Advances in Water Resources*, *24*(7), 763–774.

Kirchner, J. W. (2006). Getting the right answers for the right reasons: Linking measurements, analyses, and models to advance the science of hydrology. *Water Resources Research*, *42*(3).W03S04

Kleinhans, M. G., Bierkens, M. F. P., & van der Perk, M. (2010). HESS opinions on the use of laboratory experimentation: "Hydrologists, bring out shovels and garden hoses and hit the dirt". *Hydrological Sciences Journal*, *14*, 369–382.

Kollet, S. J., & Maxwell, R. M. (2006). Integrated surface-groundwater flow modeling: a free-surface overland flow boundary condition in a parallel groundwater flow model. *Advances in Water Resources*, *29*(7), 945–958.

Kuichling, E. (1889). The relation between the rainfall and the discharge of sewers in populous districts. *Transactions of the Ameican Society of Civil Engineers*, *20*(1), 1–56.

Kundu, P. K., Cohen, I., & Hu, H. (2008). Dynamic similarity. In *Fluid mechanics. 2004* (4th ed., Chapter 8, pp. 262–276). San Diego, CA: Elsevier Academic Press.

Lapides, D., David, C., Sytsma, A., Dralle, D., and Thompson, S. (2020). "Convergence and divergence on idealized hillslopes: supplementary datasets and code. https://doi.org/10.5281/zenodo.3517298, published at https://github.com/lapidesd/Hillslope_Storage_Kinematic_Wave.

Lighthill, M. J., & Whitham, G. (1955). On kinematic waves i. flood movement in long rivers. *Proceedings of the Royal Society of London. Series A. Mathematical and Physical Sciences*, *229*(1178), 281–316.

Manoj, K. C., Fang, X., Yi, Y.-J., Li, M.-H., Thompson, D. B., & Cleveland, T. G. (2013). Improved time of concentration estimation on overland flow surfaces including low-sloped planes. *Journal of Hydrologic Engineering*, *19*(3), 495–508.

Maxwell, R. M. (2013). A terrain-following grid transform and preconditioner for parallel, large-scale, integrated hydrologic modeling. *Advances in Water Resources*, *53*, 109–117.

Meyer, L., & Harmon, W. (1979). Multiple-intensity rainfall simulator for erosion research on row sideslopes. *Transactions of the ASAE*, *22*(1), 100–0103.

Moore, I. D., Hirschi, M. C., & Barfield, B. J. (1983). Kentucky rainfall simulator. *Transactions of the ASAE*, *26*(4), 1085–1089.

Morgali, J. R. (1970). Laminar and turbulent overland flow hydrographs. *Journal of the Hydraulics Division*, *96*(2), 441–460.

Mulvaney, T. J. (1851). On the use of self-registering rain and flood gauges in making observations of the relations of rainfall and flood discharges in a given catchment. *Proceedings of the Institution of Civil Engineers Ireland*, *4*, 19–31.

Noël, P., Rousseau, A. N., Paniconi, C., & Nadeau, D. F. (2014). Algorithm for delineating and extracting hillslopes and hillslope width functions from gridded elevation data. *Journal of Hydrologic Engineering*, *19*(2), 366–374.

Petroselli, A. (2012). Lidar data and hydrological applications at the basin scale. *GIScience & Remote Sensing*, *49*(1), 139–162.

Poff, N. L., Allan, J. D., Bain, M. B., Karr, J. R., Prestegaard, K. L., Richter, B. D., … Stromberg, J. C. (1997). The natural flow regime. *Bioscience*, *47*(11), 769–784.

Shelton, C. H., von Bernuth, R. D., & Rajbhandari, S. P. (1985). A continuous-application rainfall simulator. *Transactions of the ASAE*, *28*(4), 1115–1119.

Tarolli, P., & Dalla Fontana, G. (2009). Hillslope-to-valley transition morphology: New opportunities from high-resolution dtms. *Geomorphology*, *113*, 47–56.

Thompson, S., Katul, G., Konings, A., & Ridolfi, L. (2011). Unsteady overland flow on flat surfaces induced by spatial permeability contrasts. *Advances in Water Resources*, *34*(8), 1049–1058.

Troch, P., van Loon, E., & Hilberts, A. (2002). Analytical solutions to a hillslope-storage kinematic wave equation for subsurface flow. *Advances in Water Resources*, *25*(6), 637–649.

Troch, P. A., van Loon, A. H., & Hilberts, A. G. J. (2004). Analytical solution of the linearized hillslope-storage Boussinesq equation for exponential hillslope width functions. *Water Resources Research*, *40*(8), W08601.

White, F. M. (1999). *Fluid mechanics* (4th ed.New York, New York: ). WCB/McGraw-Hill.

Woolhiser, D. A., & Liggett, J. A. (1967). Unsteady, one-dimensional flow over a plane—The rising hydrograph. *Water Resources Research*, *3*(3), 753–771.

**How to cite this article:** Lapides DA, David C, Sytsma A, Dralle D, Thompson S. Analytical solutions to runoff on hillslopes with curvature: numerical and laboratory verification. *Hydrological Processes*. 2020;1–20. https://doi.org/10.1002/hyp.13879

## APPENDIX I. ADDITIONAL DETAILS ON PARFLOW SIMULATIONS A.

In order to minimize any differences between ParFlow simulations and analytical solutions due to numerical error, we checked that the ParFlow simulations were stable with respect to a change in space or time discretization to ensure that, to as great a degree as possible, deviation between the two models is due primarily to the simplicity of the analytical solutions. We ran initial simulations using a 1 m spatial grid and a 0.01 hr timestep for three test hillslopes with $a = -0.02$, $a = 0$, and $a = 0.02$. We ran additional simulations with the space and time grids at 1/4, 1/2, 2× and 4× this resolution to check sensitivity of the results to the numerical grid. We tabulated peak flow values from each simulation. Peak flow predictions converged with increasing resolution, with negligible change between the 2× and 4× resolutions as shown in Figure A7. All test simulations in this study were therefore run using $\Delta x = 0.5$ m and $\Delta t = 0.005hr$ (the 2× resolution case).

Results from the full set of simulations (full details in the main text) can be found in Table A2. Comparison between ParFlow and analytical solutions were performed for both the case of $m = 2$ and $m = 5/3$, while ParFlow assumes $m = 5/3$. This difference in $m$ explains the fact that statistics for $m = 2$ are less robust than those for $m = 5/3$. The qualitative behavior of the comparisons is similar, with the same pattern of increasing or decreasing fit with value of $a$. Even without the comparison to the analytical solutions, % error $Q_{peak}$ and CV can be used to assess the likelihood that the analytical solution will provide a good fit to the numerical data. As % error $Q_{peak}$ increases, flow behavior deviates more from the expected flowlines, causing 2-D flow not accounted for in the analytical model. As CV increases, the average flow along a cross-section becomes a poorer fit to the flow. CV and % error $Q_{peak}$ both increase steadily with $|a|$ until very large values of $|a|$, where % error $Q_{peak}$ becomes small or switches sign, due to a much larger error that the statistics do not capture well. The step change above $a = |0.02|$ is apparent in the magnitude of many of the statistics.

## APPENDIX II. EXPERIMENTAL RAINFALL AND ROUGHNESS PARAMETERS B.

Rainfall intensity and roughness both had to be calibrated prior to comparison of experimental hydrographs with analytical hydrographs. Rainfall in the analytical model is assumed uniform and constant. Throughout experiments, rainfall rate varied only with small variations in tap pressure, which were mostly controlled for by a pressure reducer. Due to material limitations, though, rainfall was not uniform. Variation in the rainfall was measured in 7 independent trials. In each trial, two 4x4 grids of petri dishes were laid out on a level surface beneath the rainfall simulator for 2 min each, and the collected water weighed. The rainfall pattern was consistent across all trials, and the rainfall rate was consistent among tests performed in the same trial (average varied from 7–12 mm/hr). Variations in rainfall rate between trials are likely due to uncontrollable pressure differences in the mains water line used. Small changes in measured rainfall pattern over time were observed, and are likely due to changes in the performance of

**TABLE A1** Reference list of symbols used in text

| | |
|---|---|
| $A$ | Hillslope contributing area [$L^2$] |
| $A_{max}$ | Total hillslope area [$L^2$] |
| $a$ | Curvature parameter in exponential width function [1/$L$] |
| $C$ | Constant of proportionality so that $C = 2c$ [$L$] |
| $c$ | Constant multiplier for exponential width function [$L$] |
| $E$ | Elevation change between the divide and the outlet [$L$] |
| $f$ | Infiltration rate (constant) [$L/T$] |
| $g$ | Gravitational acceleration [$L/T^2$] |
| $H$ | Flow cross-section [$L^2$] |
| $h$ | Water depth [$L$] |
| $\bar{h}$ | Average depth [$L$] |
| $\bar{h}_*$ | Average depth on characteristic at $t_r$ [$L$] |
| $I$ | Rainfall intensity [$L/T$] |
| $k$ | Curvature parameter in conic section hillslope equation from Evans (1980) [] |
| $L$ | Hillslope length [$L$] |
| $m$ | Constant dictating flow regime [] |
| $n$ | Manning's $n$ [] |
| $Q$ | Volumetric flow rate [$L^3/T$] |
| $Q_{peak}$ | Peak flow in hydrograph [$L^3/T$] |
| $q$ | Flow per unit width [$L^2/T$] |
| $\bar{q}$ | Average flow rate along a contour [$L^2/T$] |
| $q_{peak}$ | Maximum $q$ in hydrograph [$L^2/T$] |
| $S_f$ | Friction slope [] |
| $S_o$ | Slope [] |
| $t$ | Time [$T$] |
| $t_c$ | Time of concentration [$T$] |
| $t_e$ | Time to equilibrium flow value [$T$] |
| $t_p$ | Time of ponding [$T$] |
| $t_r$ | Length of rainstorm [$T$] |
| $t_0$ | Time of start of characteristic in Domain 2 [$T$] |
| $u$ | Velocity [$L/T$] |
| $w(x)$ | Hillslope width function [$L$] |
| $x$ | Spatial coordinate pointing downhill [$L$] |
| $x_*$ | Location of characteristic at $t_r$ [$L$] |
| $x_0$ | Location of start of characteristic in Domain 1 [$L$] |
| $y$ | Cross-slope coordinate [$L$] |
| $y_1$ | Limiting flowline [$L$] |
| $y_2$ | Limiting flowline [$L$] |
| $z$ | Height of topography above a base elevation [$L$] |
| $\alpha$ | Roughness [$L^{2-m}/T$] |
| $\rho$ | Density [$M/L^3$] |
| $\xi$ | Metric defined as the RMSE between two hydrographs [] |
| $\omega$ | Cross-slope curvature parameter from Evans (1980) [ ] |

| $a$ | % error $Q_{peak}$ | CV | $\xi_{5/3}$ | $\xi_2$ | $RMSE_{5/3}$ | $RMSE_2$ |
|---|---|---|---|---|---|---|
| −0.1 | 1.21% | 0.56 | 0.052 | 0.16 | 0.76 | 2.34 |
| −0.05 | 8.58% | 0.68 | 0.037 | 0.15 | 1.19 | 2.57 |
| −0.02 | 22.18% | 0.41 | 0.018 | 0.13 | 2.86 | 3.48 |
| −0.01 | 24.91% | 0.28 | 0.012 | 0.12 | 3.15 | 3.58 |
| −0.005 | 19.24% | 0.21 | 0.011 | 0.11 | 2.44 | 3.01 |
| −0.001 | 12.60% | 0.09 | 0.011 | 0.11 | 1.59 | 2.37 |
| −0.0005 | 9.41% | 0.06 | 0.011 | 0.11 | 1.17 | 2.10 |
| −0.0001 | 4.43% | 0.03 | 0.013 | 0.11 | 0.56 | 1.81 |
| 0 | 0.00% | 0.00 | 0.014 | 0.11 | 0.21 | 1.65 |
| 0.0001 | −5.88% | 0.03 | 0.015 | 0.11 | 0.81 | 1.69 |
| 0.0005 | −8.76% | 0.06 | 0.016 | 0.11 | 1.16 | 1.77 |
| 0.001 | −10.78% | 0.08 | 0.018 | 0.11 | 1.41 | 1.86 |
| 0.005 | −18.07% | 0.14 | 0.022 | 0.11 | 2.31 | 2.32 |
| 0.01 | −17.83% | 0.17 | 0.022 | 0.11 | 2.25 | 2.25 |
| 0.02 | −9.51% | 0.20 | 0.019 | 0.10 | 1.21 | 1.65 |
| 0.05 | 31.54% | 0.20 | 0.035 | 0.08 | 4.39 | 3.85 |
| 0.1 | 1.48% | 0.22 | 0.041 | 0.03 | 15.06 | 13.33 |

**TABLE A2** Summary of results from numerical simulations in ParFlow (Jones and Woodward (2001), Jones and Woodward (2001) Kollet and Maxwell (2006), Maxwell (2013)). The percent errors in $q_{peak}$ is shown between the numerical simulations and the expected value of $A_{max}$ * $I$. CV is the coefficient of variance in flow along the bottom boundary at the time of equilibrium flow. The metric $\xi$ is the RMSE between hydrographs normalized by peak flow. The subscripts on $\xi$ and RMSE indicate the $m$ value used for the comparison to ParFlow

**TABLE A3** Fitted roughness $\alpha$ values for laboratory experiments. Fits are shown only for trials that passed quality control. At the top, fitted values are shown for $a$ equal to the value in the first column. Below, fitted values are calculated under the assumption that $a$ = 0 in all cases

| $a$ | Trial Number | $\alpha$ |
|---|---|---|
| Curvature-included fit | | |
| 0.05 | 3 | 5.53 |
| | 4 | 8.59 |
| 0.0 | 3 | 8.29 |
| | 4 | 8.59 |
| −0.05 | 1 | 18.39 |
| | 3 | 14.41 |
| No-Curvature fit | | |
| 0.05 | 3 | 9.82 |
| | 4 | 12.88 |
| 0.0 | 3 | 8.29 |
| | 4 | 8.59 |
| −0.05 | 1 | 14.71 |
| | 3 | 12.27 |

the atomizing nozzles over time or incidental adjustment of the locations of petri dishes used for measurement. The observed rainfall pattern shows two primary nodes of rainfall, as demonstrated in Figure A8, which shows the average rainfall pattern across all 7 trials. Rainfall was observed across the full hillslope surface in each experimental run, although the amount of rainfall clearly varies to a great degree. The coefficient of uniformity is on average 17%. This is a fairly low value, indicating that the rainfall from our constructed rainfall simulator is highly variable. For comparison, other rainfall simulators have been found to achieve 70–94% coefficient of uniformity (e.g., Esteves et al., 2000; Humphry et al., 2002; Meyer & Harmon, 1979; Moore et al., 1983; Shelton et al., 1985), about 4–5 times better than the rainfall simulator constructed for this experiment. The effective rainfall rate calibrated from experimental hydrographs was near 10 mm/hr in all cases, very close to the average rainfall intensity measured in these trials.

Roughness $\alpha$ is also calculated from experimental hydrographs rather than measured directly. As a result, the value of $\alpha$ depends on the scale factor, $a$, and the effective rainfall intensity. Calculated roughness values for each trial and the average value for each $a$ are reported in Table A3. The values of $\alpha$ vary with $a$ for the curvature-included fit so that the smallest $\alpha$ values are measured for the most divergent hillslopes. This may be incidental, though. We did our best to match surface treatment among all hillslopes, but the amount of sand that adhered to glue may have varied among the hillslopes. Prior to the first model runs, we rinsed down each hillslope to remove any sand or dust that was not adhered to prevent error in the conversion from weight to mass. This also may somehwat be a function of scale since the scale values for $a$ = 0.05 and $a$ = 0 (1:40) are the same in the table, while a smaller scale is used for $a$ = − 0.05 (1:30). For the no-curvature fit, though the $\alpha$ values are comparable, although the $a$ = 0 values are the smallest, and $a$ = − 0.05 are still the largest.

Despite difficulties in parameterizing the analytical solutions, the NRMSE between the rising limbs of the analytical and experimental hydrographs is very high. This indicates that, although the falling limbs of the runs were qualitatively similar to the eye, there was sufficient information to select different alphas that allowed for excellent fit of the rising limb and time to equilibrium.

**TABLE A4** Table of compared smoothing methods applied to volume-time curves. *f* refers to the fraction of nearest neighbors used in the kernel, *d* refers to the degree of polynomial regression, and *t* to the number of residual-based reweightings. Superscript 1 is attributed to Cleveland (1979)

| | Name | *f* | *d* | *t* |
|---|---|---|---|---|
| 1 | moving average without reweightings | 0.05 | 0 | 0 |
| 2 | linear locally-weighted regression without reweightings | 0.04 | 1 | 0 |
| 3 | linear locally-weighted regression with three residual-based reweightings (robust locally-weighted regression)[1] | 0.03 | 1 | 3 |
| 4 | quadratic locally-weighted regression without reweightings | 0.08 | 2 | 0 |

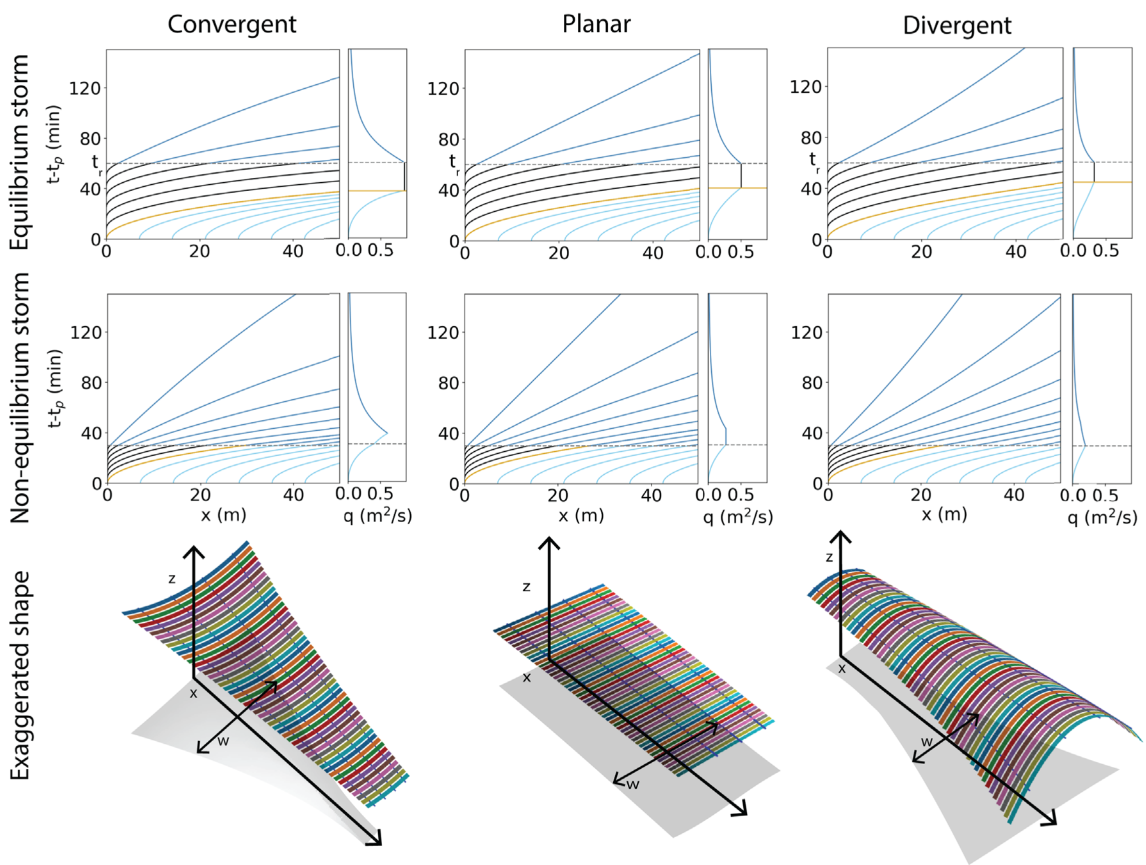


**FIGURE A1** Sample characteristic nets for (left) a convergent hillslope with $a = -0.02$, (center) a planar hillslope, and (right) a divergent hillslope with $a = 0.02$ under two different storm scenarios with no infiltration. The hillslope shapes are shown below the nets. The characteristic shown in gold is the first originating from the top of the hillslope to reach the outlet. Its passage through ($x = L$) marks the time of equilibrium flow $t_e$, shown as a solid gray line in each hydrograph panel. Domain 1 (the rising limb) is shown in light blue, Domain 2 (equilibrium flow) in black, and Domain 3 (the falling limb) in dark blue. The rising limb is steeper in the convergent hillslope hydrographs than the divergent ones, and the recession steepest for the divergent hillslopes. 46

## APPENDIX III. QUALITY ASSURANCE FOR EXPERIMENTAL HYDROGRAPHS C.

Computation of raw experimental results yielded noisy hydrographs, so smoothing was required for rigorous comparison with the analytical model. Sources of noise in the raw data included: small pooling and outburst events in the trough, slight movement of the collection beaker, or other jumps resulting from the resolution of the digital scale (± 0.025 g). These sources of error are minimal enough to produce visually smooth volume-time curves but great enough to impede visual analysis of hydrographs computed directly from raw data. The raw data consisted of cumulative mass time series of water collected every second at the outlet of the experimental models. Raw data were converted to volume time series with an assumed water density of 1.0 kg/m$^3$. The hydrograph is given by the derivative of the volume-time curve.

Prior to computing derivatives, for optimal results, we smoothed the volume-time curves by 4 methods that employ locally-weighted regression (LOWESS) with a tricubic kernel, for which the fraction of nearest points was visually tuned for each method to achieve smooth, yet accurate hydrographs. The methods are distinguished based on three parameters: *f* refers to the fraction of nearest neighbors used in

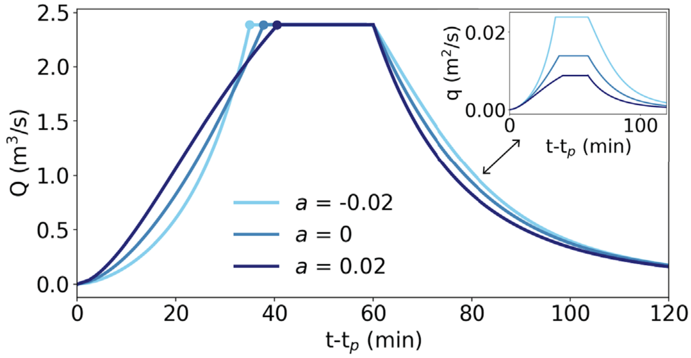


**FIGURE A2** Hydrographs produced using Equations (14), (16), (20), (22), (27), and (29) for a 60 min storm with no infiltration on three hillslopes of identical area and length: convergent $a = -0.02$ (light blue), uniform width $a = 0$ (medium blue), and divergent $a = 0.02$ (dark blue). The time of equilibrium $t_e$ is marked with a dot for each hillslope. There is a 20% difference in $t_e$ between the convergent and divergent cases. The inset shows flow rate $q$ ($m^2/s$). Flow rate differs by a factor of 2 between convergent and divergent cases. 47

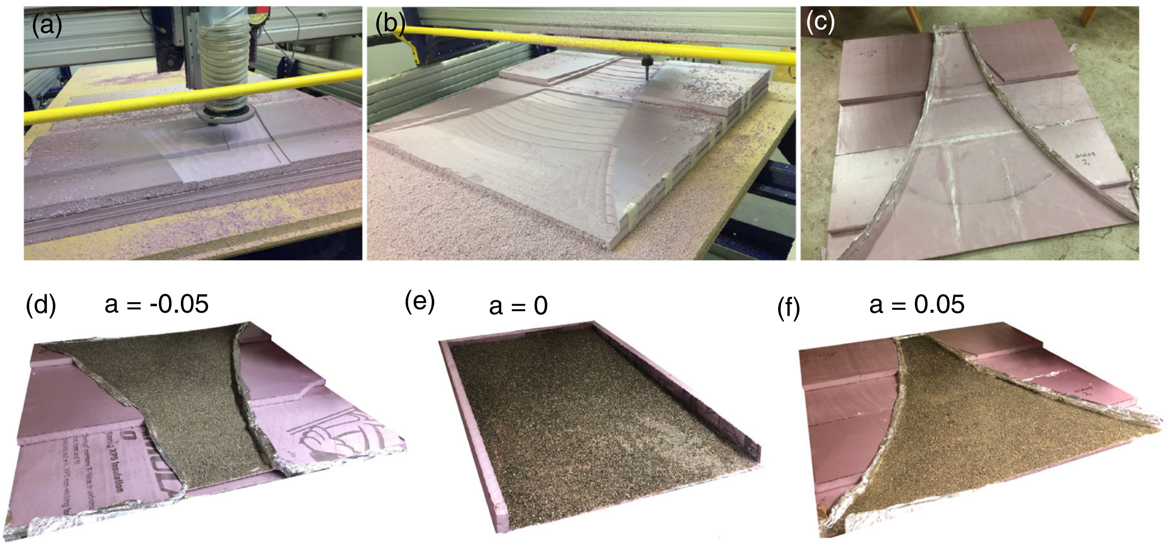


**FIGURE A3** (a) First step of CNC fabrication and (b) second step of CNC fabrication of engineered hillslope. (c) Smooth surface finish with cracks filled in using insulation foam and epoxy, sanded flat to the surface. Aluminum is used to line the edges of the model. The lower half of the figure shows completed models after the application of sand to the surface to increase hydrophilicity. 48

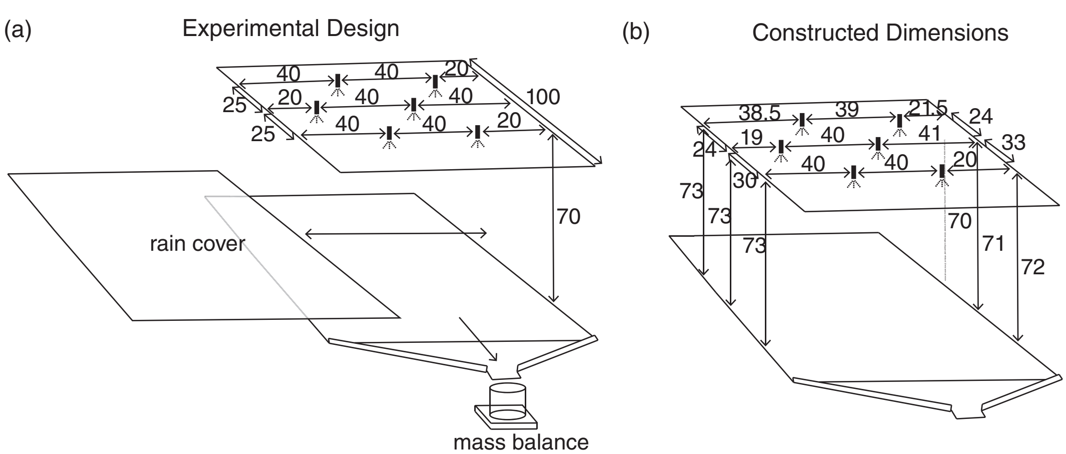


**FIGURE A4** (a) Diagrams of planned experimental design with dimensions in cm. Atomizing nozzles are marked by black rectangles with dashed lines indicating spray. (b) The actual constructed dimensions of the experiment are shown. Errors are due to material limitations, measurement error, or accidental changes made to the position of the rainfall simulator throughout experimentation and nozzle replacement. 49

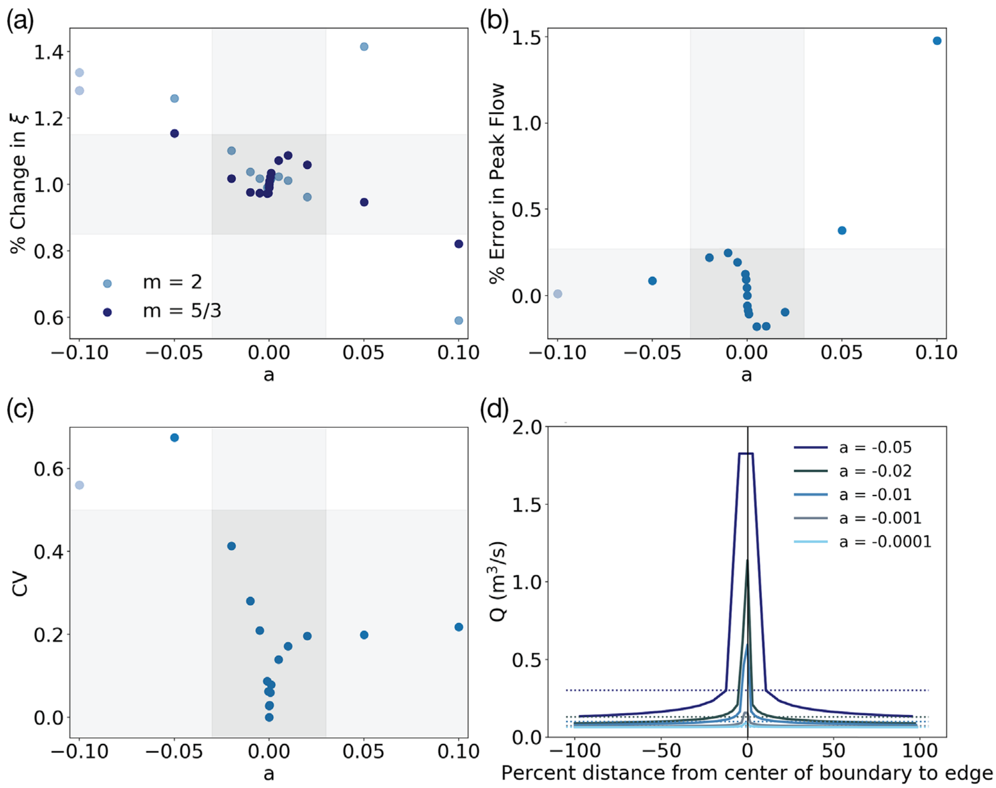


**FIGURE A5** Sample data from numerical simulations. $a = -0.1$ data is shown in grey due to low confidence in statistics. Data are shown in comparison to $m = 5/3$ solutions only since qualitative results are very similar for $m = 2$. In panels (a), (b), and (c), shaded regions indicate (horizontal bars) the region of acceptable values for the given statistic and (vertical bars) the region identifying the values of $a$ that consistently exhibit appropriate values for the statistics. (a) $\xi$ normalized by the value of $\xi$ at $a = 0$ for $m = 2$ and $m = 5/3$. Absolute magnitudes are larger for $m = 2$, as shown in Table 2. (b) Large errors in maximum flow (compared to expected mass balance $AI$) indicate 2-D flow behavior not described by the analytical solution presented in this study. (c) CV remains below small for all divergent runs but increases steadily for convergent simulations due to increased flow concentration. (d) Flow cross-sections along the bottom boundary for convergent hillslopes diverge more from the average (dotted line) as $a$ increases. Deviation from symmetry (vertical line for comparison) in (d) occurs when flow is routed to one of two equivalent center grid points. 50

the kernel, $d$ refers to the degree of polynomial regression, and $t$ to the number of residual-based reweightings (Cleveland, 1979). The names and descriptions of the methods are found in Table A4. Smoothed volume-time curves were converted to hydrographs using central differences in the interior and one-sided differences at the boundaries. This process yielded 4 different smoothed hydrographs and one unsmoothed hydrograph. The unsmoothed hydrograph was very noisy since finite differences amplify noise in the data, as shown for the example dataset in Figure A9 (b). Figure A9 shows the evaluation workflow for one dataset, which is completed for all 12 sets and summarized in Figure A10.

Results of the different smoothing methods were evaluated by (1) a Roughness Index and (2) the root mean squared error (RMSE) of each smoothed volume-time curve from the corresponding raw (unsmoothed) volume-time curve. We define the Roughness Index as the mean frequency of concavity reversal, since we expect visually rough curves to reverse concavity more frequently than visually smooth curves. To calculate this index, we first compute the second derivatives of each smoothed hydrograph. We then compute a power spectral density estimate of the second derivative curve and take the (power-weighted) average frequency of the spectrum. Figure A9 (c) shows a close-up of the second derivative curves and their power spectra for an example dataset. Conceptually, a "period" of the second derivative curve is the time it takes for the hydrograph to go from concave to convex to concave again, so a concavity reversal occurs in half of this "period". Thus we define the Roughness Index as twice the power spectrum's average frequency, which is equal to the mean frequency of concavity reversal.

It is expected that poorly smoothed hydrographs should have a high Roughness Index and over-smoothed volume-time curves should differ significantly from the raw data (i.e., high RMSE). For the best result, both the Roughness Index and the RMSE are minimized.

Out of all 4 smoothing methods, quadratic local regression (method 4 in Table A4) has, on average, the lowest Roughness Index and the lowest RMSE, as shown in Figure A10. For all experimental data, quadratic local regression has, on average, a mean frequency of concavity reversal that is 0.88 standard deviations below the mean and an RMSE that is 0.94 standard deviations below the mean, as indicated by the purple triangle in Figure A10. By these standards of

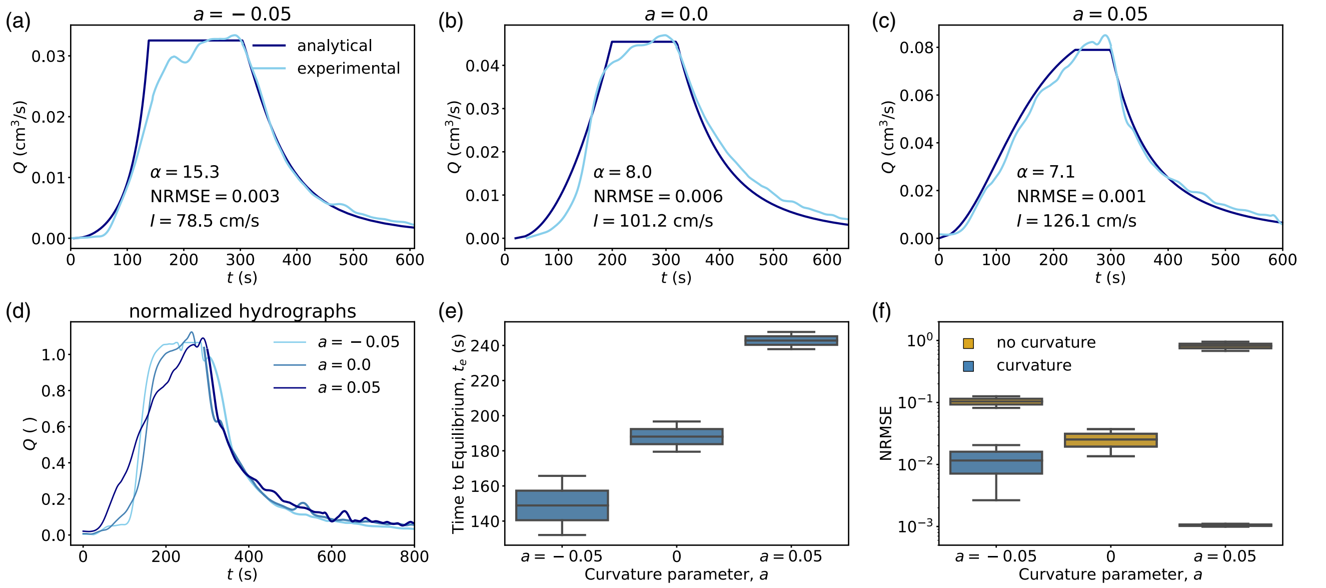


**FIGURE A6** Sample experimental hydrographs (light blue) are plotted with parameterized analytical solutions (dark blue) for (a) $a = -0.05$, (b) $a = 0$, and (c) $a = -0.05$. (d) Normalized experimental hydrographs for $a = -0.05$, $a = 0$, and $a = 0.05$ plotted together to demonstrate the differences in rising limb behavior. A boxplot of (e) time to equilibrium ($t_e$) demonstrates high confidence in the qualitative trend in $t_e$ predicted by the analytical solutions. (f) shows a plot of NRMSE between the rising limbs of analytical (for curvature-included (blue) and curvature-removed (orange) models) and experimental results (normalized by peak flow) to demonstrate the quality of the fit produced by the analytical solutions and the improvement offered by including curvature in the model. For $a = 0$, the boxes are plotted on top of one another since results for curvature and no curvature are identical. 51

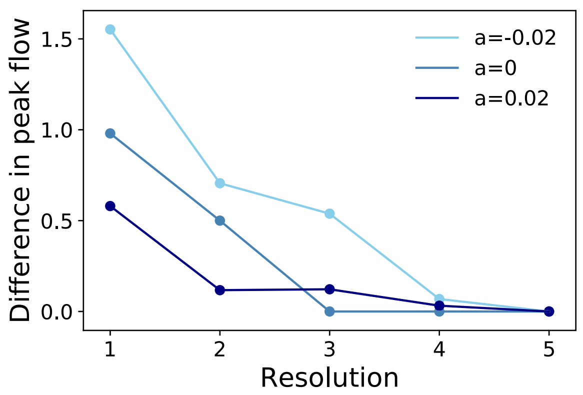


**FIGURE A7** Difference in peak flow values between simulations at different resolutions and the highest-resolution simulation (0.25) in $m^3/s$. The resolutions on the x-axis refer to the ratio between the base resolution and the tested resolution from 1/4 to quadruple (4). As resolution increases (moving right), the difference in peak flow approaches 0. For all values of $a$, the difference in peak flow for 0.5 resolution is nearly 0, so we determine that double resolution is adequate to control numerical dispersion and diffusion. 52

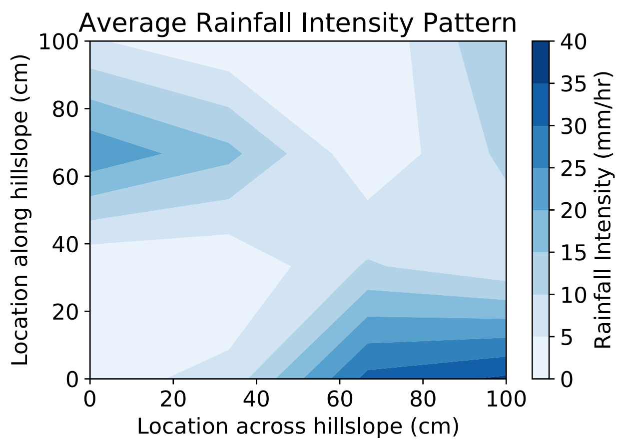


**FIGURE A8** Average rainfall intensity pattern above the hillslope model. Black dots mark locations of rain depth measurement. Approximate diagonal symmetry may allow for less strong impact on experiment results than would be expected for 17% coefficient of uniformity. 53

smoothness and fit, quadratic locally-weighted regression with a tricubic kernel is the best smoothing method for these data.

To produce final hydrographs, all datasets were smoothed using quadratic locally-weighted regression (method 4). The quality of each dataset was then assessed through visual inspection with the expectation of a smooth rising limb, peak, and falling limb. Many of the datasets had superimposed structure that deviated greatly from this form, which likely resulted from observed perturbations to the experimental set-up. These events, which included spilling, outbursts from pools, and leaks (that were subsequently patched), were clearly expressed in the smooth hydrographs. Out of the 12 runs, 6 problematic datasets were visually identified and discarded, leaving 2 runs for each hillslope.

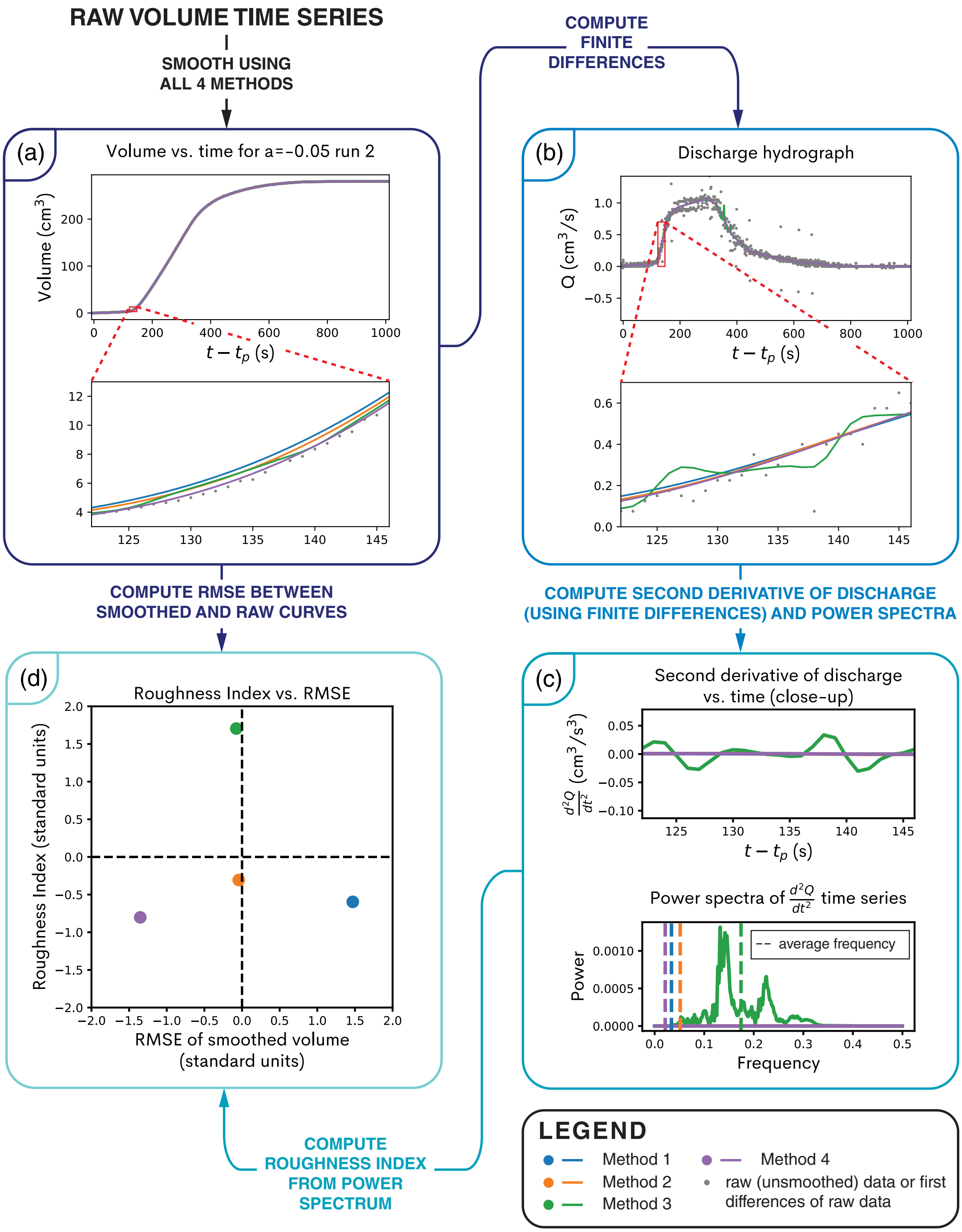


**FIGURE A9** Workflow for the comparative evaluation of smoothing methods for an example dataset (a = –0.05, run 2). (a) Raw data is smoothed by the methods described in Table A4, which produce distinguishable curves shown in the close-up. (b) Finite differences are computed from the smoothed and raw volume-time curves to produce the hydrographs shown. (c) The second derivatives of the 4 smooth hydrographs are computed, and their power spectra are estimated. (d) The Roughness Index is computed from the average frequency of each power spectrum and scattered against the RMSE between smoothed and raw volume-time curves. Values are plotted in standard units (standard deviations away from the mean value for each method), that allow for relative comparison between methods. The best method is the one with the lowest Roughness Index and lowest RMSE 54

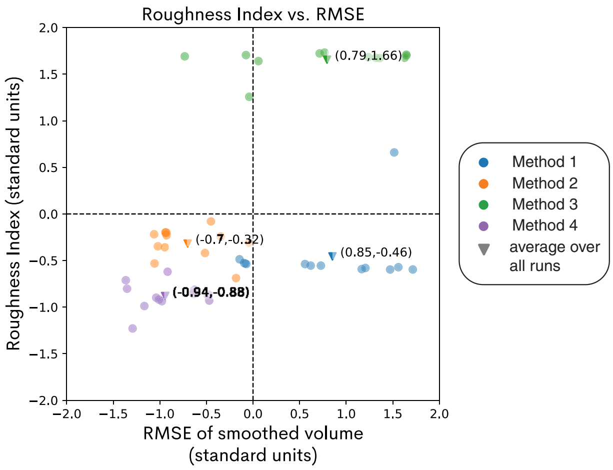


**FIGURE A10** Scatter of Roughness Index vs. RMSE of the smoothed volume-time curves for all 12 datasets. Points are plotted for each of the smoothing methods in Table 4. Values are shown in standard units (standard deviations away from the mean value from each run). Quadratic local regression (method 4) has, on average, the lowest Roughness Index (average 0.88 standard deviations below the mean) and the lowest RMSE (average 0.94 standard deviations below the mean) for each run, as shown by the purple triangle in the lower left corner. 55